ScienceAdvances

AAAS

Supplementary Materials for

Rainfall regimes of the Green Sahara

Jessica E. Tierney, Francesco S. R. Pausata, Peter B. deMenocal

This PDF file includes:

Supplementary Materials and Methods

1. Core sites & chronologies

The four cores used in this study were collected in 2007 from the *R/V Oceanus* as part of the Changing Holocene Environments in the Eastern Tropical Atlantic (CHEETA) cruise (OCE437-7; Fig. 1). The chronology of each core is based mainly on ^{14}C dating of the planktonic foraminifer *Globigerina bulloides*, although for some intervals mixed planktonic species were used due to low abundance (c.f. ref. 10). Age models for these cores were published previously *(10)* but are updated here with the addition of several new dates (table S1) and recalibration with the Marine13 radiocarbon curve *(64)*. Following ref. 10, we used the P_Sequence routine in OxCal 4.2 *(65, 66)* to construct the age models, with an additional reservoir correction (ΔR) of 130±25 years (1σ) based on locally-observed reservoir ages *(67)* and the k parameter set to 0.75. Figure S7 shows the resulting age models.

2. Organic geochemical analyses

2.1. Sampling and preparation

The cores were sampled for analyses every 3–4 cm. Wet sediments were freeze-dried, homogenized, and then extracted using an accelerated solvent extractor (ASE) 350 at a temperature of 100°C and maximum pressure of 1500 psi. The resulting total lipid extracts (TLEs) were evaporated to dryness using N_2 gas then purified using column chromatography. TLEs were separated into neutral and acid fractions over LC-NH$_2$ gel using CH_2Cl_2:isopropanol (2:1) and 4% acetic acid in ethyl ether as the respective eluents. The acid fraction was then methylated (heated to 50°C, overnight) using acetyl chloride-acidified GC grade methanol of a known isotopic composition. The methylated fatty acids (fatty acid methyl esters; FAMEs) were further purified over silica gel using hexane and CH_2Cl_2 as respective eluents. The CH_2Cl_2 fraction, containing the FAMEs, was dried under N_2 gas and then redissolved in hexane for analysis by gas chromatography.

2.2. Analyses

The hydrogen and carbon isotopic compositions of the FAMEs were measured via gas chromatography-pyrolysis-isotope ratio monitoring mass spectrometry (GC-IR-MS) using a Thermo Finnigan Delta V Plus mass spectrometer. H_2 and CO_2 gases calibrated to an authentic n-alkane standard (the "A5" mix, provided by Arndt Schimmelmann at Indiana University) were used as a working references for each analysis. In addition, an internal standard (*cis*-11-eicosenoic acid) was added to each sample after extraction but before purification, and a synthetic mix of FAMEs was analyzed every 10 samples to monitor drift and correct for any offsets. Samples were run at least in duplicate and typically in triplicate. The standard error of repeat analyses (precision) was 2‰ or better for δD and 0.2‰ or better for δ^{13}C. We applied mass balance corrections

for the addition of the methyl group during the methylation, where δD_{meoh} was determined to be -83±1‰ and $\delta^{13}C_{meoh}$ was determined to be -42.7±0.5‰ by repeat measurements of a phthalic acid standard of a known isotopic composition (provided by Arndt Schimmelmann at Indiana University) methylated with the same methanol used for the methylation of the target compounds.

We analyzed the fatty acids, as opposed to the n-alkanes, in the west African margin sediments because they were more abundant and easier to purify for GC-IR-MS measurements. We measured the C_{30} fatty acid as the representative terrestrial leaf wax (hereafter, δD_{wax}) due to evidence that fatty acids of shorter chain lengths could potentially have a competing aquatic origin in the marine environment (68).

Figure S8 shows the δD_{wax} and $\delta^{13}C_{wax}$ data for each core site.

3. Inferring δD_P and Precipitation from δD_{wax}

3.1. Modeling δD_P from δD_{wax}

Studies of leaf wax isotopic fractionation across different plant types show that the isotopic difference between δD_{wax} and δD_P ($\varepsilon_{water-wax}$) may differ by plant life form and photosynthetic pathway (21,69,70). In particular, monocots (grasses) tend to have more negative $\varepsilon_{water-wax}$ than dicots (shrubs and trees), possibly due to systematic differences in leaf-water enrichment as new waxes are produced at leaf flush (21,71).

Present-day vegetation near our core sites consists of Mediterranean, Saharan and Sahelian taxa, including C_4 grasses and C_3 shrubs/trees, as well as some C_4 shrub species. It is very likely that this vegetation assemblage changed in the past in response to Green Sahara climatic conditions. To assess the impact that changing vegetation may have on $\varepsilon_{water-wax}$ and δD_{wax}, we measured both δD_{wax} and $\delta^{13}C_{wax}$ in modern core top sediments, also collected during the CHEETA cruise, spanning the range of our proxy sites as well as a variety of vegetative and climatic zones (fig. S9). Comparison of core top δD_{wax} to estimates of δD_P derived from the OIPC (Online Isotopes in Precipitation Calculator) product (61) indicates that δD_P can only account for 40% of the variance in δD_{wax} data (fig. S1a). This suggests that vegetation composition or other factors additionally influence δD_{wax} along the west African margin.

Previous paleoclimate studies have successfully used paired $\delta^{13}C_{wax}$ measurements to account for the impact of changing vegetation composition on $\varepsilon_{water-wax}$ (22,72,73). To test whether $\delta^{13}C_{wax}$ information can aid in the prediction of δD_P, we developed a simple model

$$\delta D_P = \frac{1000 + \delta D_{wax}}{\frac{\varepsilon_p}{1000} + 1} - 1000, \tag{1}$$

$$\varepsilon_p = f_{C4} \times \varepsilon_{C4} + (1 - f_{C4}) \times \varepsilon_{C3}$$

ε_{C4} and ε_{C3} are average $\varepsilon_{water-wax}$ values for C$_4$ plants and C$_3$ dicots, respectively, taken from the compilation of ref. 21 (table S2). We modeled f_{C4} from coretop $\delta^{13}C_{wax}$ using Bayesian inference and Monte Carlo sampling of observed end-member C$_4$ and C$_3$ $\delta^{13}C_{wax}$ distributions. As a plant wax can be assumed to come from either from a C$_4$ or C$_3$ plant, the likelihood of a C$_4$ plant wax (Y) given a certain f_{C4} (θ) is a binomial distribution

$$p(Y|\theta) = \binom{N}{Y} \theta^Y (1 - \theta)^{N-Y} \tag{2}$$

Y, the number of observed C$_4$ plant waxes in N samples, is calculated from the core top $\delta^{13}C_{wax}$ and average $\delta^{13}C_{wax}$ end-member values for C$_4$ plants and C$_3$ dicots

$$Y = \left(\frac{\delta^{13}C_{wax} - \delta^{13}C_{C3}}{\delta^{13}C_{C4} - \delta^{13}C_{C3}} \right) N \tag{3}$$

N is assumed to be large, since core top $\delta^{13}C_{wax}$ represents the average value of thousands of wax compounds from either a C$_3$ or C$_4$ plant. For simplicity, we assume $N = 1000$.

End-member $\delta^{13}C_{wax}$ values are taken from the "All Africa" compilation of ref. (74) (table S2). This compilation includes a diverse range of plant species found in arid and mesic areas of central and east Africa and thus should be representative of taxa found in the Sahara and Sahelian environments. We note that, like the end-member $\varepsilon_{water-wax}$ values, these values are for the C$_{29}$ n-alkane, not the C$_{30}$ n-acid that we have analyzed in the sediments. Unfortunately, comparable end-member data for the C$_{30}$ n-acid do not exist; hence, we use data for the closely-related C$_{29}$ n-alkane compound. Although some systematic differences between n-alkanes and n-acids have been observed, uncertainties surrounding these differences are large (75) and it is not known whether these offsets apply to African taxa. Therefore, in the absence of further information, we assume that n-alkane and n-acid endmember distributions for both $\delta^{13}C_{wax}$ and $\varepsilon_{water-wax}$ are similar.

The data in the "All Africa" compilation are corrected for the Suess effect – the ca. 1‰ change in atmospheric CO$_2$ due to the burning of fossil fuels. We do not, however, correct our coretop data for the Suess effect, because bioturbation modeling suggests that the Suess signal would be effectively mixed with underlying sediments at the sedimentation rates of our core sites, and reduced to ca. 0.2‰ in magnitude. This is equivalent to the standard error of our analyses;

thus we do not expect the Suess effect to be distinguishable from analytical noise.

Returning to the inference of f_{C4}, what we seek is calculation of $p(\theta|Y)$: f_{C4} conditional on the observed C_4 plant waxes. According to Bayes' Rule

$$p(\theta|Y) \propto p(Y|\theta)p(\theta) \tag{4}$$

where $p(\theta)$ is the prior distribution. The conjugate prior for a binomial likelihood is a beta distribution

$$p(\theta) = \theta^{\alpha-1}(1-\theta)^{\beta-1} \tag{5}$$

In this case, we choose as our prior $\alpha = 1$ and $\beta = 1$, or rather, a uniform distribution over the interval (0,1).

The posterior distribution is also a beta distribution

$$p(\theta|Y) \propto \theta^{Y+\alpha-1}(1-\theta)^{N-Y+\beta-1} \tag{6}$$

Calculation of $p(\theta|Y)$, the posterior distribution of f_{C4}, then proceeds by 1) sampling the C_4 and C_3 $\delta^{13}C_{wax}$ end-member values from normal distributions with a mean and standard deviation according to the values in table S2; 2) calculating Y; and 3) sampling the posterior beta distribution. We then calculate $\varepsilon_{water-wax}$ and δD_P from Equation (1), employing Monte Carlo sampling of both the $\varepsilon_{water-wax}$ end-member distributions (table S2) and the δD_{wax} measurements ($\sigma = 2‰$) to propagate uncertainties.

Figure S1b shows the results of this modeling process. Regression analysis demonstrates that predicted δD_P exhibits a strong relationship with OIPC δD_P (with 74% of the variance explained) falling nearly on the one-to-one line with a slope indistinguishable from 1 and an intercept indistinguishable from 0. The core-top exercise therefore validates the use of our simple δD_P model (Eq. 1) to predict δD_P from δD_{wax} values and confirms that $\delta^{13}C_{wax}$ information is needed to account for changing $\varepsilon_{water-wax}$ across the dynamic landscapes along the West African margin.

We apply the same modeling approach to the downcore data to predict δD_P. However, to isolate the hydroclimatic component of the δD_{wax} signal, we first correct the δD_{wax} data for ice volume effects. To correct for ice volume changes, we assume a Last Glacial Maximum change in global $\delta^{18}O$ of seawater of 1‰ (76) and scaled the benthic oxygen isotope stack (77) – a proxy for the changes in global ice volume – accordingly. We then removed the ice volume

change from the data using the following equation

$$\delta D_{wax-corr} = \frac{1000 + \delta D_{wax}}{8 \times 0.001 \times \delta^{18}O_{ice} + 1} - 1000 \tag{7}$$

Figure S8 shows the ice-volume δD_{wax} data alongside the original data for comparison.

3.2. Predicting precipitation rates from δD_P

Limited observations of water isotopes in the Sahara suggest that the "amount effect" (78) exerts a strong influence on the isotopes in precipitation, with a change of 100 mm/year corresponding to a shift in $\delta^{18}O$ of -1 to -2‰ (79). To better understand the relationship between between regional δD_P and precipitation, we study data from the derived Online Isotopes in Precipitation Calculator (OIPC) product (61), the nudged, isotope-enabled historical IsoGSM simulation (80), and our δD_{wax}-derived δD_P estimates. In all three cases, we observe a non-linear dependence of δD_P on precipitation rates across the Sahara, with a steeper slope at lower rainfall rates in agreement with expectations from Rayleigh distillation (fig. S2). IsoGSM exhibits more non-linearity in this relationship than the OIPC observations or our coretop-derived δD_P, the latter two of which are adequately described by a logarithmic relationship (fig. S2). We therefore assume that the relationship between δD_P and precipitation scales with the logarithm of precipitation, such that

$$\delta D_P = \alpha + \beta \cdot \ln(precipitation) + \epsilon, \tag{8}$$
$$\epsilon \sim \mathcal{N}(0, \tau^2) \text{ IID}$$

To derive quantities for α, β, and τ^2, we use observed precipitation values from the GPCCv6 product (60), the core top δD_{wax}-inferred δD_P values, and Bayesian regression. Priors for α, β, and τ^2 take the form of Normal, Normal, and Inverse Gamma distributions, respectively

$$\alpha \sim \mathcal{N}(\mu_\alpha, \sigma_\alpha^2) \tag{9}$$
$$\beta \sim \mathcal{N}(\mu_\beta, \sigma_\beta^2)$$
$$\tau^2 \sim \mathcal{IG}(\lambda_\tau, \eta_\tau)$$

The prior distributions are all conjugate and result in the following conditional posterior distributions

$$\alpha|\cdot \sim \mathcal{N}(\psi_\alpha \nu_\alpha, \nu_\alpha) \tag{10}$$

$$\psi_\alpha = N\tau^{-2}(\bar{Y} - \beta\bar{X}) + \mu_\alpha \sigma_\alpha^{-2}$$

$$\nu_\alpha = (N\tau^{-2} + \sigma^{-2})^{-1}$$

$$\beta|\cdot \sim \mathcal{N}(\psi_\beta \nu_\beta, \nu_\beta) \tag{11}$$

$$\psi_\beta = \tau^{-2}(X^T Y - N\alpha\bar{X}) + \mu_\beta \sigma_\beta^{-2}$$

$$\nu_\beta = (X^T X \tau^{-2} + \sigma^{-2})^{-1}$$

$$\tau^2|\cdot \sim \mathcal{IG}\left(\lambda_\tau + \frac{N}{2}, \eta_\tau + \frac{1}{2}(Y - \alpha - \beta X)^T(Y - \alpha - \beta X)\right) \tag{12}$$

where X = precipitation, $Y = \delta D_P$, and N is the number of calibration points.

Calculation of the posteriors proceeds by specifying an initial value for each unknown parameter and then implementing a Gibbs sampler (81). In addition, we sample the uncertainty in the δD_P and precipitation values by randomly drawing values from Normal distributions with means and variances equivalent to the observed errors.

Figure S10a compares the prior and posterior distributions for each of the regression parameters. In all cases, the posterior is much narrower than the prior, indicating that the data are exacting a dominant control on the posteriors.

To predict precipitation values from the δD_P time series at each core site, we employ another application of Bayes' Rule. In this case, it is necessary to specify a prior for $\mathbf{P}$, the vector of precipitation rates estimated from δD_P. Recalling that we are working in logarithmic space, the prior for each site is set as a truncated normal: $\mathbf{P} \sim \mathcal{N}_{[0,\ln(5000)]}(\mu_P, \sigma_P)$, where μ_P is set to the natural logarithm of modern mean annual precipitation rate at the core site, and $\sigma_P = 5$. The truncation is set to exclude solutions that correspond to less than 1 mm/year (equivalent to the driest place on Earth presently) and greater than 5000 mm/year (far greater than the maximum rainfall rates in the the Congo rainforest, which are ca. 3500 mm/year). The full conditional posterior is multivariate normal

$$\mathbf{P}|\cdot \sim \mathcal{N}(\psi_P \nu_P, \nu_P)$$

$$\psi_P = \sigma_P^{-1}\mu_P + \tau^{-2}\beta(\delta D_P - \alpha) \tag{13}$$

$$\nu_P = (\sigma_P^{-1} + \tau^{-2}\beta^2)^{-1}$$

Inference of precipitation then proceeds by drawing a possible δD_P time series from the ensemble produced from the approach described in Section 3.1, and then drawing from the full conditional posterior using each set of parameter values (α, β, τ^2) determined from the calibration model. However, we note that that τ^2 estimate from the spatial regression is likely an unrealistically conservative estimate for the variance of each data point from a non-independent time series; i.e., the uncertainty of each point in the time series is not the same as the uncertainty in the *mean value* of inferred precipitation. To account for this difference, we utilize τ^2 to calculate the mean values of the time series as a whole, but do not apply it to the variance of each individual point. Rather, pointwise variance corresponds to the uncertainty in the δD_P estimation only. The result is an ensemble of possible precipitation time series that accounts for the uncertainty in the calibration parameters (α and β) and in the δD_P–precipitation relationship (τ^2) in the mean value, while the variance of each point in the time series corresponds the variance derived from resampling inferred δD_P values.

Figure S10b compares the prior and posterior values for each core site, demonstrating that while the prior is somewhat informative, the posterior is narrower, indicating substantial learning from the δD_P data. Site GC37 has a bimodal distribution, which reflects the prevalence of two distinct rainfall regimes: dry regime similar to present, and a wet regime unique to the Green Sahara.

Temperature and the isotopic composition of precipitation

Precipitation and temperature are negatively correlated across our coretop transect ($r = -0.88, p < 0.001$), largely driven by the decline in temperature and increase in precipitation as the transect approaches northern Morocco and southern Spain. This makes the statistical separation and attribution of temperature vs. precipitation changes difficult. However, in tropical regions and subtropical arid locations, temperature influences on the isotopic composition of precipitation are generally considered small or insignificant, secondary to the "amount effect" (*82*). We further note that the correlation between δD_{wax}-estimated δD_P and temperature ($r = 0.56, p = 0.01$) is weaker than the correlation with precipitation ($r = -0.72, p < 0.001$). This suggests to us that precipitation changes dominate the δD_P signal, especially in the arid western Sahara.

Alkenone and foraminiferal transfer function records of temperature close to our core sites suggest a glacial–interglacial change in temperature of ca. 4–5 °C (*83, 84*). Assuming that condensation temperatures follow suit, this would correspond to a mean change in the δD_P of precipitation of -4 to -5 per mil. Given that this effect is small, and given that we cannot assume that condensation temperatures would have changed accordingly, we do not correct our δD_{wax} data for glacial–interglacial changes in temperature. Making this correction would lower precipitation estimates for the LGM and deglacial period; thus, the glacial estimates we present here can be considered maximal estimates.

4. Bioturbation modeling

Given the relatively modest sedimentation rates at our core sites (6–12 cm/ka; fig. S7) and the fact that they do not lie in oxygen minimum zones, bioturbation is expected to effect the magnitude, timing, and abruptness of major features of the inferred precipitation time series. In particular, bioturbation will alter the timing and duration of the termination of the Green Sahara and the onset of the 8 ka "pause" at our lowest latitude site (GC68), influencing our interpretation of these key events. To assess the effects of bioturbation on our data, we conducted a series of experiments with the TURBO2 bioturbation model *(58)*. TURBO2 models bioturbation as an instantaneous mixing process within a given mixing depth, which approximates most radionuclide-based bioturbation data reasonably well (*85*). TURBO2 also accounts for the noise introduced when mixing (and analyzing) limited number of "particles" (typically, foraminifera). Although our time series do not consist of a limited number of particles (a large number of leaf wax compounds are analyzed for their isotopic composition) we set the particle number to a value of 20 to simulate the noise inherent in our time series.

To approximate the time series that we observe, we conducted of series of iterative simulations with TURBO2, inputting simple step-wise functions with shifts at key locations and varying the mixing depths until a best match was found. We emphasize that the input series are not intended to be the "true" climate signal, but rather, are designed to test the hypotheses that 1) the termination of the Green Sahara was abrupt at these locations, but appears gradual due to bioturbation; 2) the termination of the Green Sahara was roughly synchronous between these sites; and 3) that an extended 8 ka dry period is needed to explain the presence of the "pause" in wet conditions at Sites GC49 and GC68. Results are shown in fig. S4. For our northernmost sites, we found that mixing depths greater than 5 cm would result in transitions that were far too abrupt to be consistent with the data. In contrast, larger mixing depths (8 and 10 cm, respectively) were required to simulate transitions at the more southerly sites. These mixing depths are reasonable: sedimentary mixing depths vary globally between ca. 0–20 cm, with an average of roughly 8 cm (*86*). Furthermore, mixing depths typically increase with increasing organic carbon flux (*87*), which supports our assumption that mixing depths are greater at the more organic-rich sites GC49 and GC68. A study of mixing depths in sediments offshore from Cap Blanc likewise suggests higher mixing rates and greater tracer penetration depth as one enters the seasonally-productive west African upwelling zone (*88*).

Our bioturbation results indicate that we cannot rule out the possibility that Green Sahara conditions ended abruptly (i.e., within a few hundred years; fig. S4). We also find that the timing of termination is similar between Sites GC37, GC49, and GC68 (pooled mean value = 5.2 ± 0.3 ka, 2σ), but significantly earlier at Site GC27 (6.5 ± 0.1 ka, 2σ; fig. S5). Our finding of a similar termination at three of the four sites agrees with a previous bioturbation analysis of dust records from these same cores *(10)*. Thus, while an early end to the Green Sahara at

Site GC27 supports the general concept of a time-transgressive termination *(23)* there is no evidence for this specifically between 19–27°N.

5.   Evidence for 8 ka drying in North and East Africa

As noted in the main text, there is widespread evidence for an interruption in Green Sahara conditions near 8,000 yr BP. Here, we compile available hydrologically-sensitive time series from North and East Africa (north of 10°S) to assess the presence and duration of the event (Table S3). We find that about 75% of the sites show evidence of 8 ka drying, with durations ranging from 400–2100 years (median = 1000 years, fig. S6). All observed durations are substantially longer that the duration of the 8.2 event in Greenland (160 years, *38*) and all but one are longer than the durations typically observed in North Atlantic climate records *(36)*. Taken together with the archaeological evidence, the ubiquity of this event lends credence to our inference that the 8 ka pause is a coherent, prolonged dry period across most of Africa.

6.   Climate model simulations

We analyzed changes in Saharan precipitation relative to pre-industrial (0 ka) conditions in an ensemble of mid-Holocene (6 ka) climate simulations performed with 31 ocean-atmosphere climate models. These simulations include Paleoclimate Modeling Intercomparison Project (PMIP) Phase 2 and 3 simulations performed by modeling centers from the USA, Japan, UK, Germany, France, China. For these simulations, orbital parameters were adjusted to match predicted 6 ka values, and trace gases were altered in accordance with ice core data *(59)*. All other boundary conditions remain the same as the preindustrial experiments. Vegetation was either prescribed at 0 ka values or interactive if a dynamic vegetation module was used, starting from 6 ka vegetation. Further details regarding the PMIP models and experimental design may be found on the PMIP website: `http://pmip3.lsce.ipsl.fr/`.

We also analyzed simulations that were recently conducted with the EG Earth model in which Green Saharan vegetation and dust were prescribed *(27)*. Three simulations were analyzed: the standard 6 ka experiment in which only orbital forcing and greenhouse gas changes are considered; an experiment in which the vegetation type over the Sahara domain (11–33°N, 15°W–35°E) is set to shrub ("Green Sahara" experiment), while the dust concentration is kept at 0 ka values; and a third experiment in which the Saharan land cover is set to shrub and the preindustrial dust flux is reduced by up to 80% (see Fig. 1 and S7 in ref. 27), based on recent estimates of Saharan dust flux reduction during the MH *(9,10)* ("Green Sahara-Reduced Dust" experiment). The vegetation change corresponds to a reduction in the surface albedo from 0.3 to 0.15 and an increase in the leaf area index from 0.2 to 2.6 (mainly desert and shrub respectively; Table 1 in ref 27). The dust reduction leads to a decrease in the dust aerosol optical depth (AOD) of almost 60% and in the global total AOD of 0.02 (see Fig. 1 in ref. 27). Initial conditions for the MH experiments were taken from a

700-year pre-industrial spin-up run, and the simulations were then run for 300–400 years. The climate reaches quasi-equilibrium after 100 to 200 years, depending on the experiment. In this paper we focus on the equilibrium responses, and only the last 100 years of each sensitivity experiment are analyzed.

Given that the GS-RD simulation best approximates the magnitude and spatial extent of the Green Sahara seen in our proxy data (Fig. 5), we used its output to investigate the seasonal changes in precipitation near 31°N, where our data from Site GC27 suggest substantially wetter conditions. We find that although there is a large reduction in sea level pressure in the eastern Atlantic at 6 ka from December–March, leading to an increase in winter precipitation in the Mediterranean region (fig. S3a), this only accounts for 10% of the annual increase at our site. Rather, abnormally high precipitation from June–September associated with the northwards expansion of the monsoon accounts for the 90% of the annual increase (fig. S3c). It is therefore not improbable that most of the inferred precipitation increase at Site GC27 was caused by changes in the latitudinal extent of the North African monsoon. The monsoonal inundation, combined with increased winter precipitation, may account for the very high (ca. 1800 mm/year; Fig. 2b) inferred annual precipitation rates at Site GC27.

Finally, we compared our inferred precipitation time series to a transient simulation spanning the last 22,000 years (TraCE-21ka) conducted with the CCSM3 climate model *(43)*. In the TraCE simulation, CCSM3 was forced by realistic insolation, atmospheric trace gases (CO_2, CH_4), continental ice sheets and meltwater discharge, as described by Liu et al. *(44)*. TraCE also included a dynamic vegetation module. As with the PMIP experiments, we find that TraCE dramatically underestimates precipitation changes in the Sahara during the Early Holocene (Fig. 3 of the main text).

Table S4 lists the models analyzed in this study, their resolution, and associated modeling center.

table S1. Radiocarbon dates for the sediment cores used in this study.

Radiocarbon dates on the CHEETA cores, analyzed at Lawrence Livermore National Laboratory, and OxCal calibrated median ages (year BP). * denote newly-added dates over the original age models of ref. 1. One date (italicized) was excluded from the GC37 age model because it would require a severe change in sedimentation rate unsupported by the lithology (c.f. ref. 1).

Depth (cm)	^{14}C Age	Error (1σ)	Age (BP)	Error (1σ)
— GC27 —				
0.5	1035	64	523	58
4.5	1790	61	1216	69
30.5	5990	35	6277	49
60.5	10390	130	11272	194
77.5	12110	60	13439	79
92.5	14800	94.5	17280	148
119.5	17240	90	20197	134
— GC37 —				
4.5	1905	61	1344	71
14.5	4100	61	3981	94
18.5	4975	58.5	5121	98
28.5	6335	35	6657	58
45.5	9740	64	10448	96
57.5	10495	50	11398	128
82.5	*14460*	*78*	—	—
119.5	14080	60	16372	126
177.5*	20790	160	24275	205
297.5*	32870	420	36641	650
— GC49 —				
4.5	1415	64	848	71
20.5	4530	70.5	4557	109
30.5	6275	64	6572	83
40.5	8045	64	8374	73
54.5	9985	61	10754	97
77.5	12120	330	12807	125
86.5	11835	64	13224	69
108.5	13125	50	14965	128
140.5	15180	121	17835	198
202	20460	110	23965	152
281.5*	27810	500	31385	485
330.5*	31500	1401	36459	996
— GC68 —				
4.5	2665	58.5	2238	76
18.5	4685	61	4740	88
26.5	5560	35	5800	56
40.5	7360	70.5	7663	71
62.5	8600	58.5	9131	88
81.5	10910	45	12079	86
90.5	10980	86	12427	97
120.5	12465	61	13853	87
144.5	13850	50	15962	95
150.5	14050	121	16283	121
167.5	14690	60	17291	109
197.5	17270	80	20121	118
251.5*	20030	120	23439	170
302.5*	22530	100	26255	147

table S2. End-member $\delta^{13}C_{wax}$ and ε values used for modeling δD_P. ε_{C4} values include both C_4 monocots and dicots, given that C_4 shrubs are present in the Sahara and Sahel. ε_{C3} values are for C_3 dicots.

| End-member	Mean	Standard Error	Source
$\delta^{13}C_{C4}$	-19.8	0.4	(74)
$\delta^{13}C_{C3}$	-33.4	0.4	(74)
ε_{C4}	-126	4	(21)
ε_{C3}	-113	2	(21)

table S3. List of paleoclimate data sets investigated for the presence of an 8 ka dry event, including their location, the type of hydrologically-sensitive proxy, approximate duration of the event, and associated references. *The duration of the 8 ka event is based on an observed lake level lowstand (89). An accompanying δD_{wax} data from the same site shows a much longer mid-Holocene decline in humid conditions that extends to ca. 5500 yr BP (23). **At Lake Tana, an 8 ka pause is evident in Ti XRF data (90) but not in δD_{wax} data (91).

| Site Name	Longitude	Latitude	Proxy	8 ka event?	Duration	References
GC27	-10.630	30.880	δD_{wax}	no	N/A	This study
GC37	-15.118	26.816	δD_{wax}	no	N/A	This study
GC49	-17.854	23.206	δD_{wax}	yes	1400	This study
GC68	-17.282	19.363	δD_{wax}	yes	2100	This study
Gulf of Aden	44.3	11.955	δD_{wax}	yes	1500	(11)
Lake Tanganyika	29.833	-6.7	δD_{wax}	yes	700	(92)
Lake Challa	37.7	-3.317	δD_{wax}, BIT	no	N/A	(93, 94)
Congo Basin	11.222	-5.588	δD_{wax}	no	N/A	(57)
Sahel	-17.948	15.498	δD_{wax}	yes	1100	(28)
Lake Bosumtwi*	-1.417	6.5	lake level	yes	1000	(89)
Lake Abhe	41.833	11.083	lake level	yes	800	(95)
Lake Ziway-Shala	38.3	7	lake level	yes	1200	(96)
Bahr El Ghazal	17	18	lake level	yes	800	(97)
Lake Turkana	36	3.5	lake level	yes	1100	(98)
Fachi-Dogonboulo	12.5	18	lake level	yes	n.d.	(99)
Kawar-Bilma	12.92	18.73	lake level	yes	1000	(99, 100)
Sebhka Mellala	5.2	32.18	stratigraphy	yes	400	(101)
Lake Victoria	33	-1	diatoms and δD_{wax}	no	N/A	(102, 103)
Hasi el Mejnah	2.5	31.66	diatoms, $\delta^{18}O$	yes	700	(79, 104)
Wadi Haijad	-3.33	22.57	diatoms, stratigraphy	yes	n.d.	(79)
Izoudene	9.22	19.53	stratigraphy	yes	900	(79)
Bougdouma	11.66	13.3	stratigraphy, $\delta^{18}O$	no	N/A	(101)
Lake Tana**	37.25	12	Ti concentration	yes	1000	(90)

table S4. List of the climate models used for model-data comparison.

List of the PMIP2 and PMIP3 climate models used for the analyses of mid-Holocene (6 ka) vs. preindustrial (0 ka) changes in precipitation in the Sahara ,including the resolution of the atmospheric component of the model. *indicates that the model contains a dynamic vegetation module.

Model Name	Institution	Country	Resolution (Lat × Lon)
— **PMIP2** —			
CCSM3	National Center for Atmospheric Research	USA	$2.8° \times 2.8°$
CSIRO-Mk3L-1.1	Commonwealth Scientific and Industrial Research Organisation	Australia	$3.19° \times 5.625°$
ECBILT-CLIO-VECODE	Koninklijk Nederlands Meteorologisch Instituut	The Netherlands	$5.6° \times 5.6°$
ECBILT-CLIO-VECODE-v*	Koninklijk Nederlands Meteorologisch Instituut	The Netherlands	$5.6° \times 5.6°$
FOAM	Argonne National Laboratory	USA	$4.4° \times 7.5°$
FOAM-v*	Argonne National Laboratory	USA	$4.4° \times 7.5°$
GISS modelE	NASA Goddard Institute for Space Studies	USA	$4° \times 5°$
HadCM3M2	Met Office Hadley Centre	UK	$2.5° \times 3.75°$
HadCM3M2-v*	Met Office Hadley Centre	UK	$2.5° \times 3.75°$
IPSL-CM4-V1-MR	Institut Pierre-Simon Laplace	France	$2.5° \times 3.75°$
MIROC3.2	Japan Agency for Marine-Earth Science and Technology, University of Tokyo	Japan	$2.8° \times 2.8°$
MRI-CGCM2.3.4fa	Meteorological Research Institute	Japan	$2.8° \times 2.8°$
MRI-CGCM2.3.4fa-v*	Meteorological Research Institute	Japan	$2.8° \times 2.8°$
MRI-CGCM2.3.4nfa	Meteorological Research Institute	Japan	$2.8° \times 2.8°$
MRI-CGCM2.3.4nfa-v*	Meteorological Research Institute	Japan	$2.8° \times 2.8°$
— **PMIP3** —			
BCC CSM1.1*	Beijing Climate Center, China Meteorological Administration	China	$2.8° \times 2.8°$
CCSM4	National Center for Atmospheric Research	USA	$1° \times 1.25°$
CNRM-CM5	Centre National de Recherches Meteorologiques	France	$1.4° \times 1.4°$
FGOALS-g2*	LASG, Chinese Academy of Sciences	China	$1.66° \times 2.81°$
FGOALS-s2*	LASG, Chinese Academy of Sciences	China	$1.66° \times 2.81°$
GISS-E2-R	NASA Goddard Institute for Space Studies	USA	$2° \times 2.5°$
HadGEM2-CC*	Met Office Hadley Centre	UK	$1.25° \times 1.875°$
HadGEM2-ES*	Met Office Hadley Centre	UK	$1.25° \times 1.875°$
IPSL-CM5A-LR*	Institut Pierre-Simon Laplace	France	$1.9° \times 3.75°$
MIROC-ESM*	Japan Agency for Marine-Earth Science and Technology, University of Tokyo	Japan	$2.8° \times 2.8°$
MPI-ESM-P	Max Planck Institute for Meteorology	Germany	$1.8° \times 1.875°$
MRI-CGCM3	Meteorological Research Institute	Japan	$1.125° \times 1.125°$
— **EC-Earth** —			
EC-Earth v3.1	Koninklijk Nederlands Meteorologisch Instituut	Japan	$1.125° \times 1.125°$
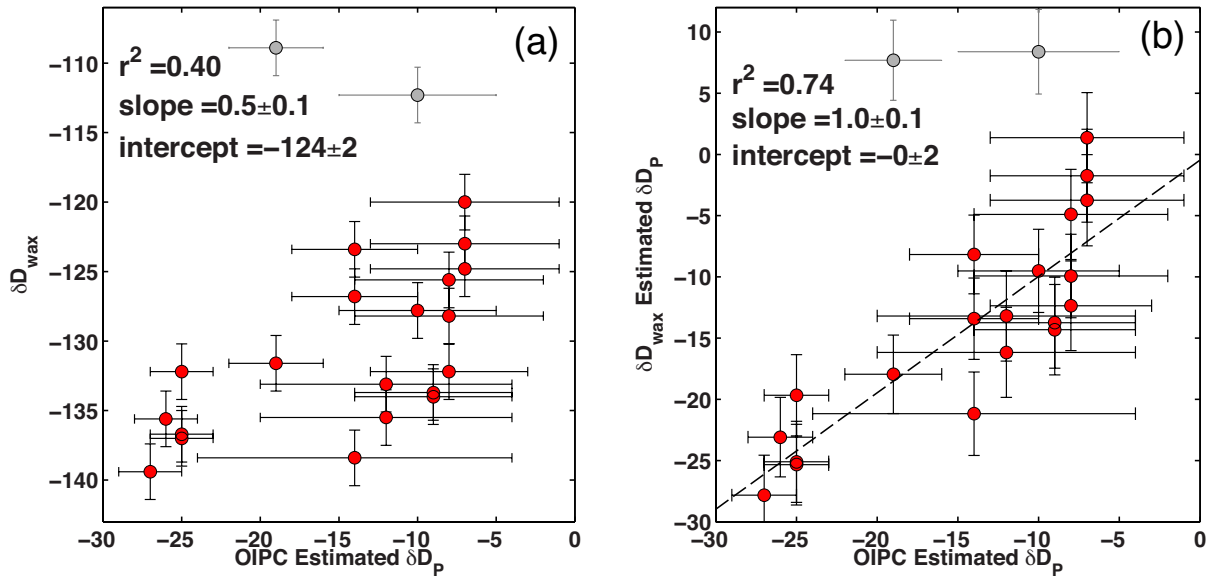
fig. S1. Estimated values for δDP versus δD$_{\text{wax}}$ and δD$_{\text{wax}}$ inferred δDP.
(a) OIPC estimates of δD_P vs. core-top values of δD_{wax}. (b) OIPC estimates of δD_P vs. modeled δD_P from δD_{wax} and $\delta^{13}C_{wax}$. Error bars denote 1σ errors. Gray points are outliers and are excluded from the calculation of the regression statistics.
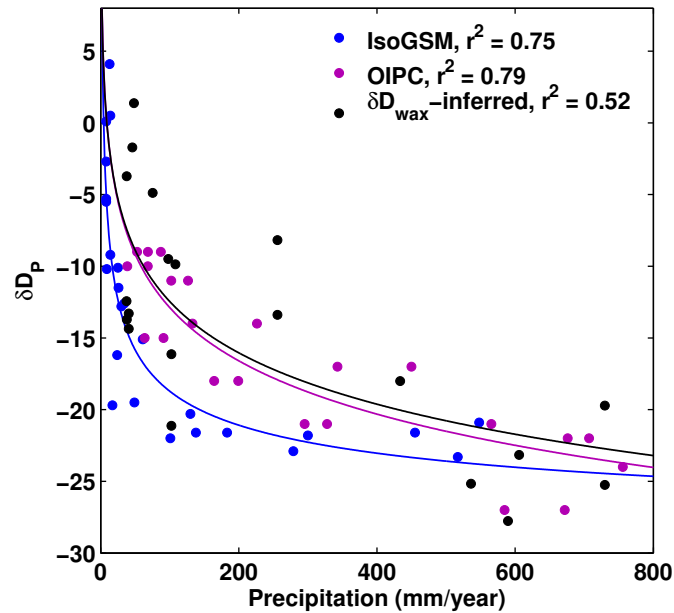

fig. S2. Regional relationship between δDP and precipitation amount.
δD_P vs. precipitation for the IsoGSM historical simulation, the OIPC interpolated product, and δD_{wax}-inferred δD_P from the CHEETA cruise coretops. Data are from coastal regions along west Africa, from 14–38°N. Precipitation values for the OIPC and δD_{wax} datasets are from the GPCCv6 product *(60)*. Lines show the best non-linear fits to the data.
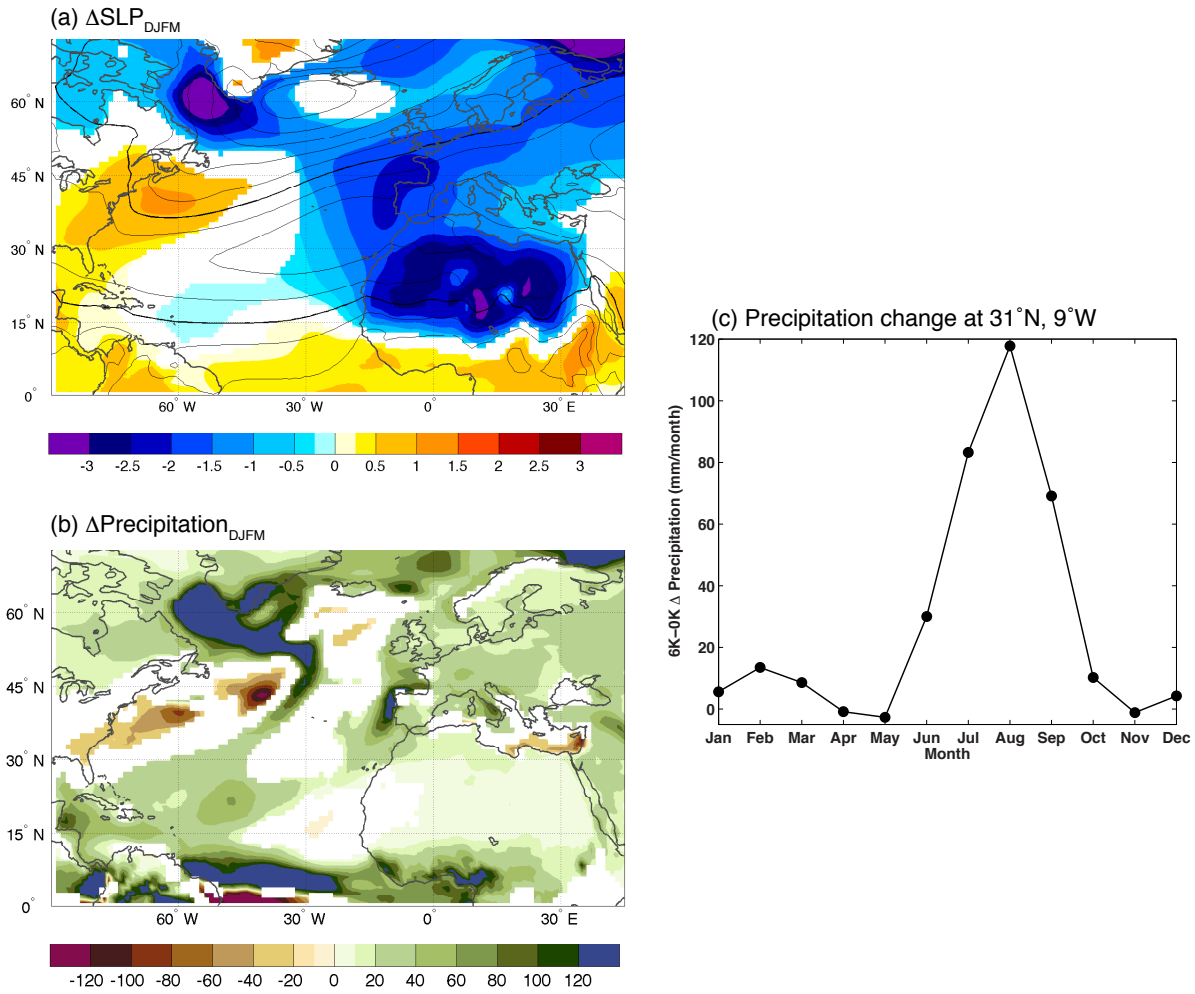
fig. S3. Changes in sea level pressure (SLP) and precipitation between the "Green Sahara-Reduced Dust" and preindustrial simulations of ref. 27. (a) Simulated change in sea level pressure (SLP) during the winter rainy season in the Mediterranean (DJFM). (b) Simulated changes in precipitation during the winter rainy season in the Mediterranean (DJFM, mm/month). (c) Simulated change in monthly precipitation rates at 31°N, 9°W (the land grid cell closest to Site GC27).
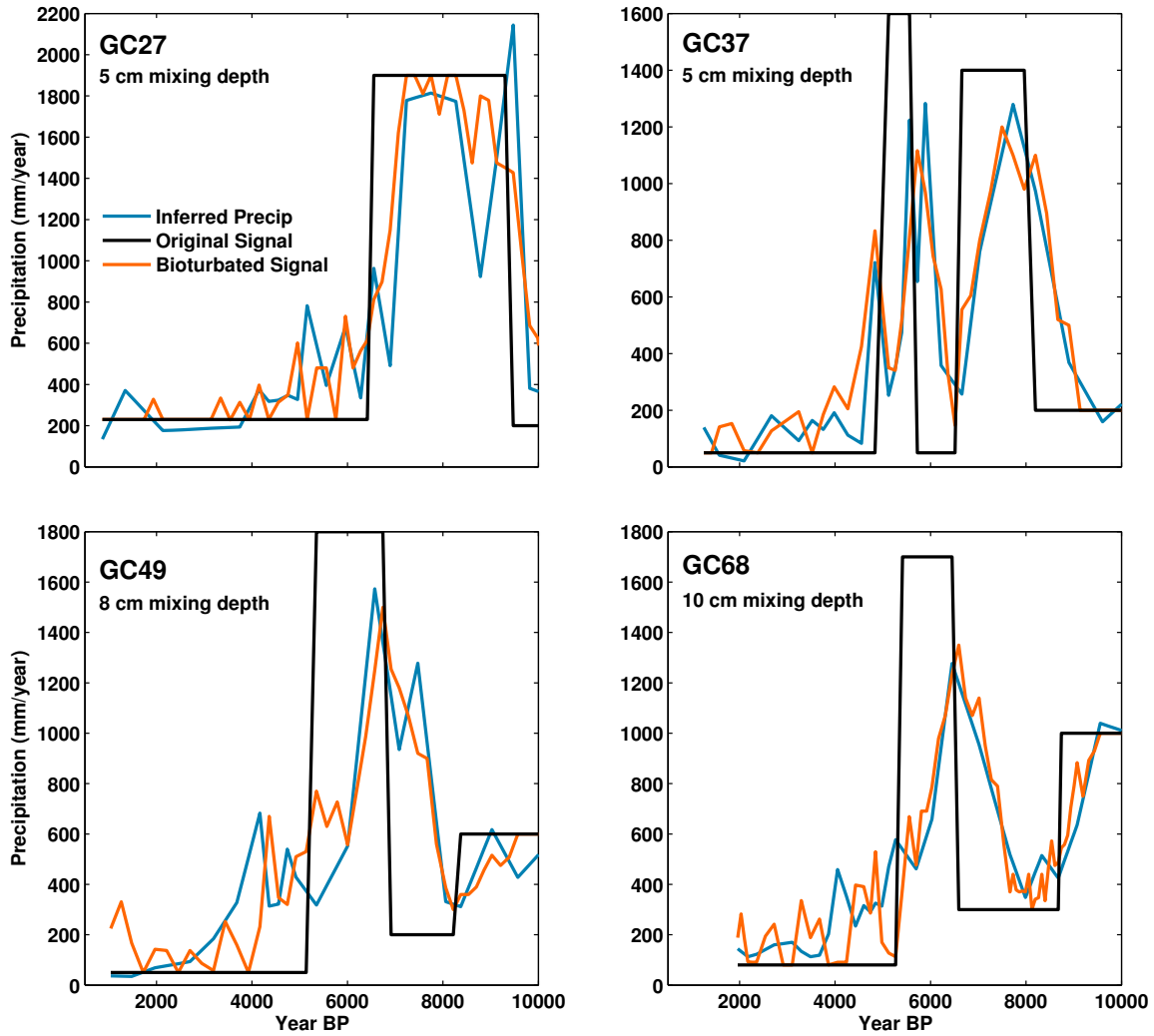
fig. S4. Bioturbation forward modeling experiments, utilizing TURBO2 *(58)*. Blue lines represent the actual data from each site; i.e., the median inferred precipitation from the leaf wax isotopes. Black lines represent the input signals for the TURBO2 model, and orange lines represent the bioturbated output from TURBO2. Mixing depths are noted in the upper lefthand corner of each panel.
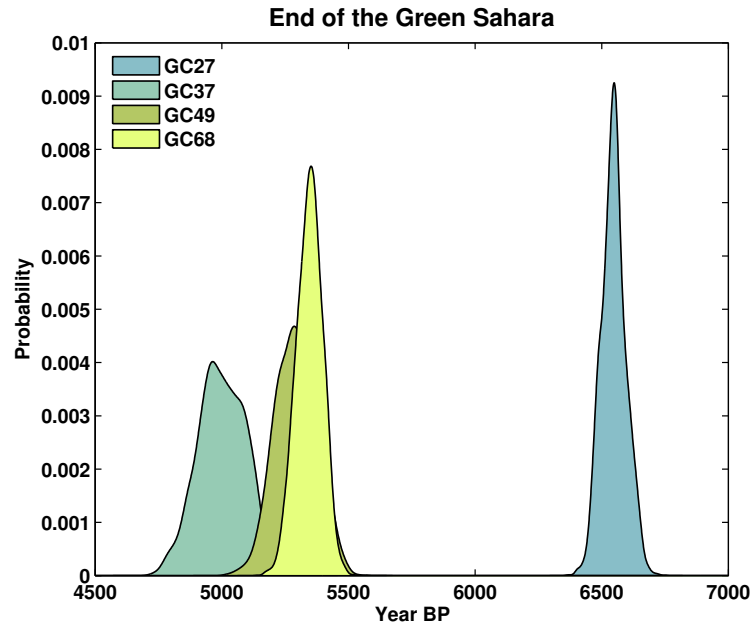
fig. S5. Probability distributions of the end of the Green Sahara at each of the four core sites, based on the inferred location in the core for an abrupt shift (according to the bioturbation modeling) and Monte Carlo iteration of the age modeling uncertainties.
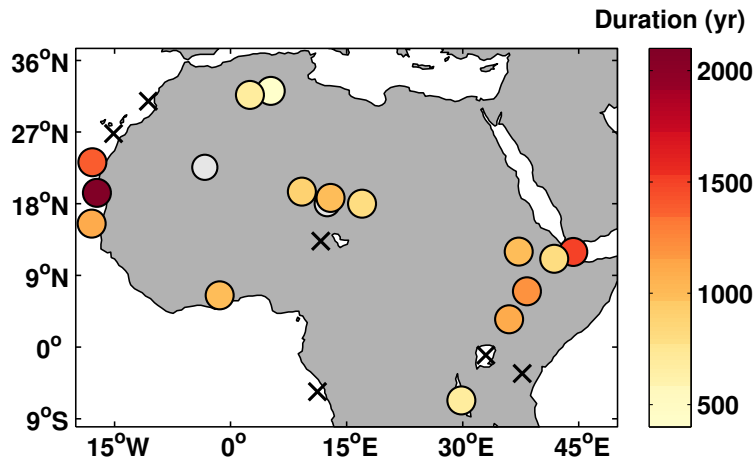
fig. S6. The presence and duration of the 8 ka dry period in paleoclimate data from North and East Africa. Colored circles denote sites where an 8 ka dry event is found and a duration could be estimated; colors indicate the approximate duration of the event (rounded to the nearest 100 years). Gray circles denote sites where an 8 ka dry event is found but the duration could not be estimated. Sites marked with an X indicate that no dry period is evident, in spite of well resolved data. See Table S3 for a complete list of the sites.
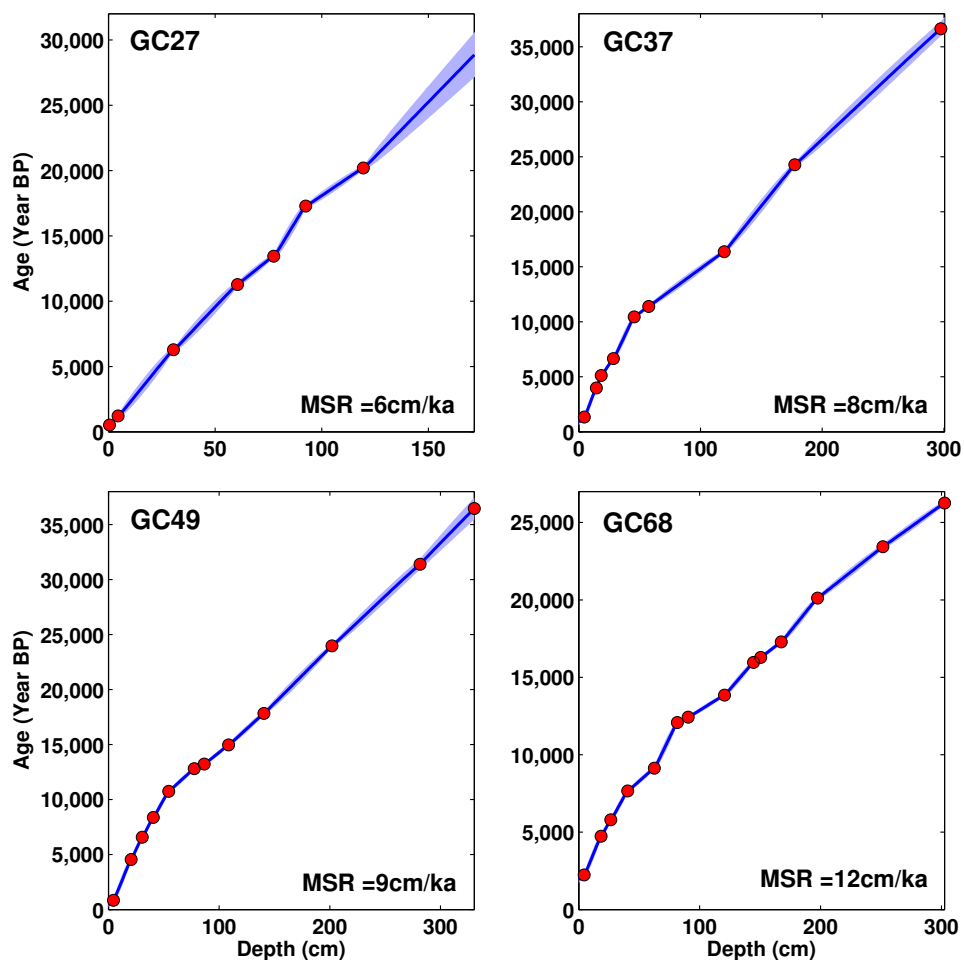
fig. S7. Age models for each of the core sites. Dated intervals are plotted in red with the median age model plotted in blue. Light blue error bars denote 1σ uncertainties. Mean sedimentation rate (MSR) is displayed in each corner of the plot.
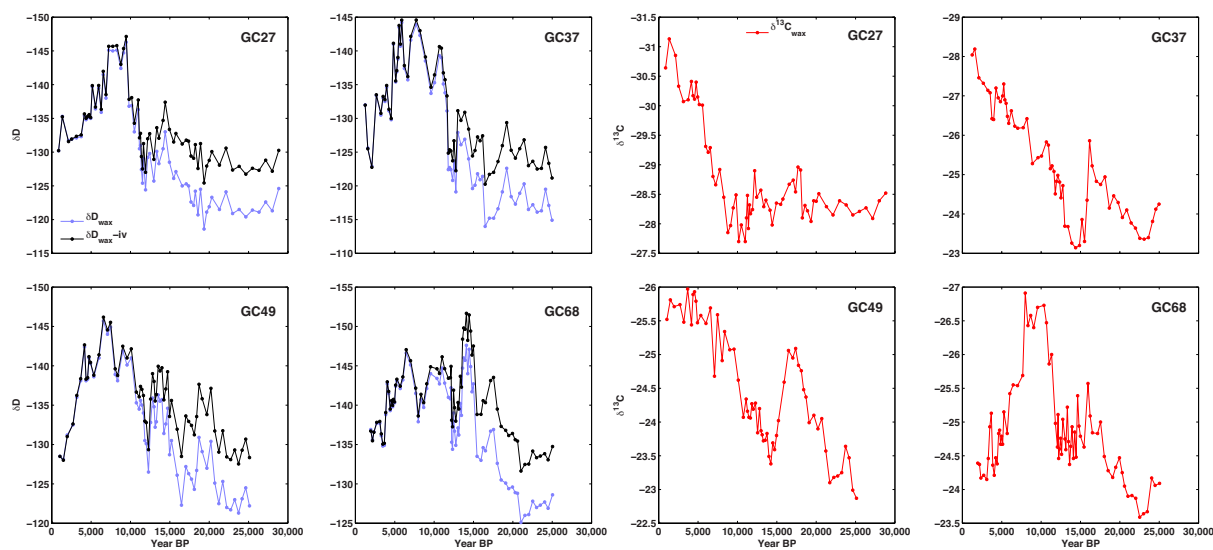
fig. S8. δD_{wax} and $\delta^{13}C_{wax}$ for each of the core sites.

At left (in blue and black), δD_{wax} data from each core site, as well as timeseries corrected for ice volume contributions (δD_{wax}-iv). The δD_{wax}-iv timeseries is used for inference of δD_P and precipitation. At right (in red), $\delta^{13}C_{wax}$ data from each core site.
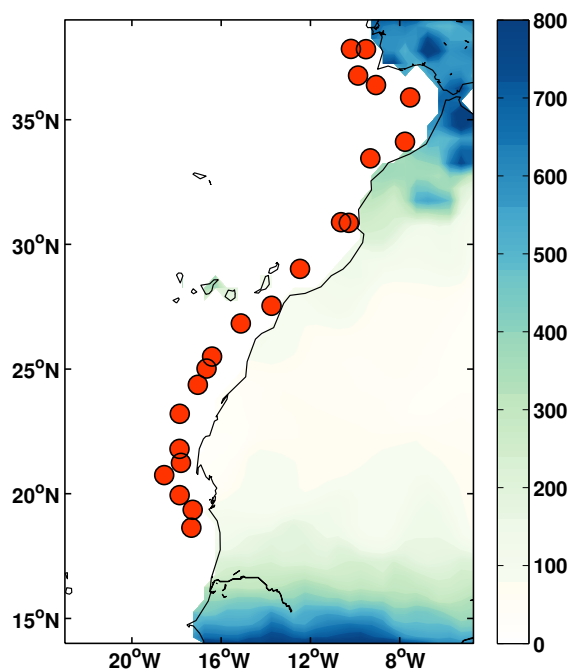
fig. S9. Map of the core top sediments used for δD_P validation and the precipitation regression model. Blue colors denote mean annual precipitation values from ref. 60.
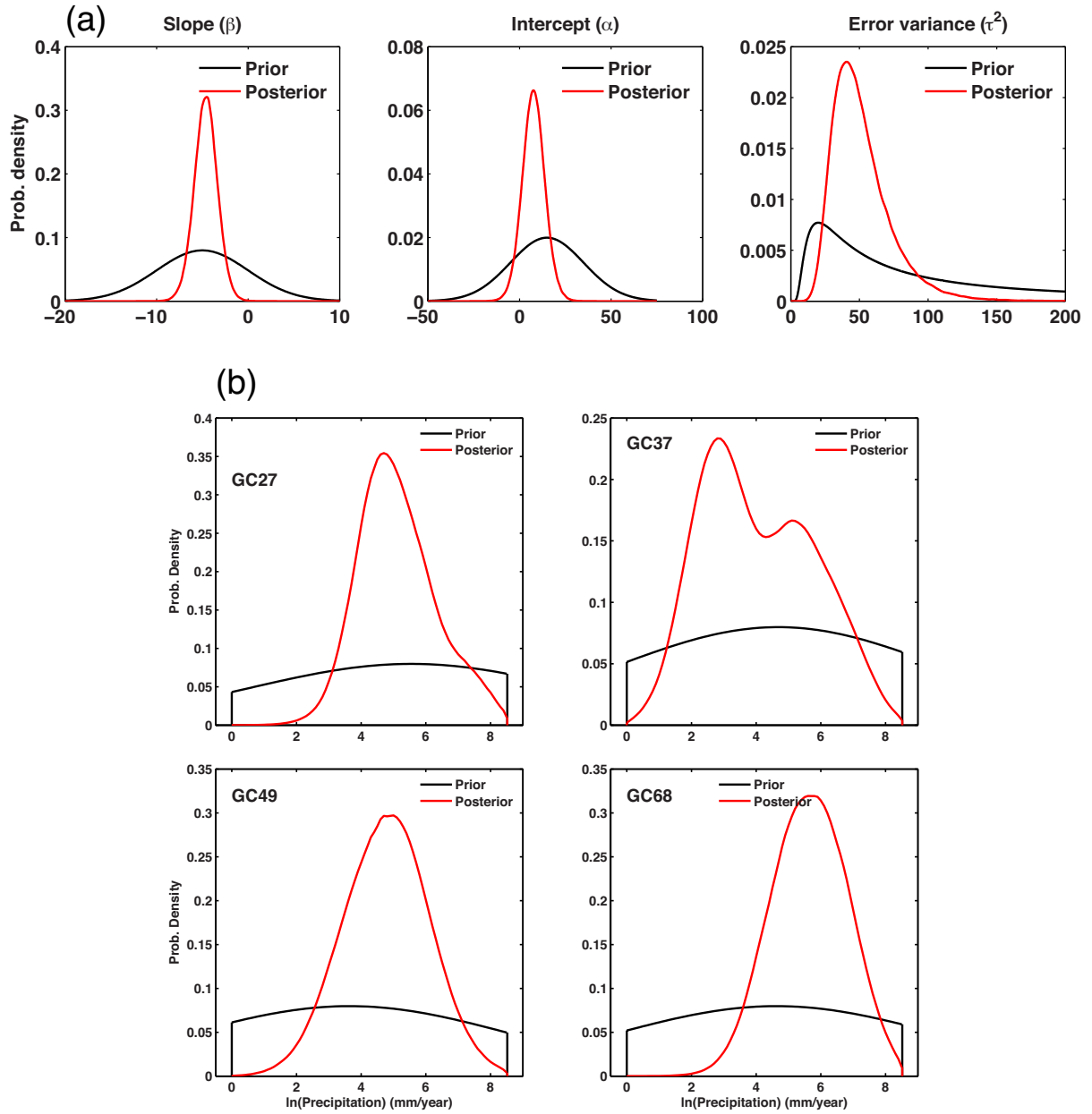
fig. S10. Prior and posterior probability distributions for the parameters of the Bayesian regression model.
(a) Prior and posterior probability distributions for the parameters of the Bayesian regression of precipitation and δD_P (Eq. 8). (b) Prior and posterior probability distributions for the inference of precipitation rates at each core site. Note x-axis is in units of ln(precipitation).